Quantifying the effects of slit confinement on polymer knots using the tube model

Yongjian Zhu, Haoqi Zhu, Fujia Tian, Qiyuan Qiu, and Liang Dai[*]

Department of Physics, City University of Hong Kong, Kowloon, Hong Kong, 999077, China
and Shenzhen Research Institute, City University of Hong Kong, Shenzhen 518057, China

Knots can spontaneously form in DNA, proteins, and other polymers and affect their properties. These knots often experience spatial confinement in biological systems and experiments. While confinement dramatically affects the knot behavior, the physical mechanisms underlying the confinement effects are not fully understood. In this work, we provide a simple physical picture of the polymer knots in slit confinement using the tube model. In the tube model, the polymer segments in the knot core are assumed to be confined in a virtual tube due to the topological restriction. We first perform Monte Carlo simulation of a flexible knotted chain confined in a slit. We find that with the decrease of the slit height from $H = +\infty$ (the 3D case) to $H = 2a$ (the 2D case), the most probable knot size L^*_{knot} dramatically shrinks from $(L^*_{\text{knot}})_{3D} \approx 140a$ to $(L^*_{\text{knot}})_{2D} \approx 26a$, where a is the monomer diameter of the flexible chain. Then we quantitatively explain the confinement-induced knot shrinking and knot deformation using the tube model. Our results for $H = 2a$ can be applied to a polymer knot on a surface, which resembles DNA knots measured by atomic force microscopy under the conditions that DNA molecules are weakly absorbed on the surface and reach equilibrium 2D conformations. This work demonstrates the effectiveness of the tube model in understanding polymer knots.

I. INTRODUCTION

Knotting is a common phenomenon in linear objects, not only macroscopic ropes [1–4], but also DNA [5–9], proteins [10–18], and other polymers [19,20]. Due to the prevalence of knotting, knots make impacts on many occasions. Knotting affects many biological processes, such as DNA replication [21] and catalysis of proteins [22]. Knotting can dramatically slow down the relaxation of a compressed polymer [23], the stretching kinetics of a polymer [24]. Knotting dramatically reduces the critical pulling force to break a polymer, because knotting causes additional strains at boundaries of polymer knots [25–27]. Knots also slow down or jam DNA nanopore translocation [28–32] and viral ejection of DNA [33,34].

DNA knots as well as single DNA molecules often experience spatial confinement in biological systems, experiments, and simulation models [20,35–43]. In some viruses, the spatial confinement from virial capsids greatly enhances DNA knotting probability to about 95% and strongly affects knot spectrum [33,34]. In experiments, nanofluidic and microfluidic channels are often used to observe knots in confined long DNA molecules [36,38,39,44–46]. The effects of spatial confinement on knotting are often nontrivial and nonmonotonic due to the competition of physical interactions and topological constraints [20,41,42,47,48].

To deeply understand polymer knots in confinement and rationally control polymer knots by confinement, one has to reveal physical mechanisms underlying the effects of confinement on polymer knots. In principle, these mechanisms might be unveiled through the statistical mechanical calculation of polymer knots. However, the conformational space for polymer knots is so complex that it is impractical to perform rigorous calculation of the integral over the ensemble of knotted conformations. Furthermore, the spatial confinement adds extra complexity into such calculation. Considering these difficulties, the theoretical treatment of polymer knots in confinement should make some approximation to simplify the problem.

In this work, we apply the tube model to understand the polymer knots confined in a slit, i.e., between two parallel plates. In the tube model, the polymer segments in a knot core are assumed to be restricted within a virtual tube due to topological entanglements. The tube model presents a simplified view of knotted polymer conformations that appear irregular and disordered. Furthermore, the tube model converts a complicated knotting problem to a virtual-tube confinement problem, which can be tackled more from theory. The idea of describing polymer knots by virtual tubes was first proposed by Grosberg, Feigel, and Rabin [49,50]. The tube model for polymer knots has been further developed by us in recent years [48,51–53]. In particular, we have developed a computational algorithm to materialize and visualize the tubes for polymer knots, which allows us to quantify the tube diameters and tube shapes and perform the calculation of other physical quantities based on these tube parameters [54,55]. In this work, we will first quantify the effects of slit confinement on polymer knots and then explain these effects using the tube model. With the slit height decreasing from $+\infty$ to about zero, the confined polymer gradually changes from the 3D case to

*liangdai@cityu.edu.hk

Free space, $L^*_{knot} = 140a$
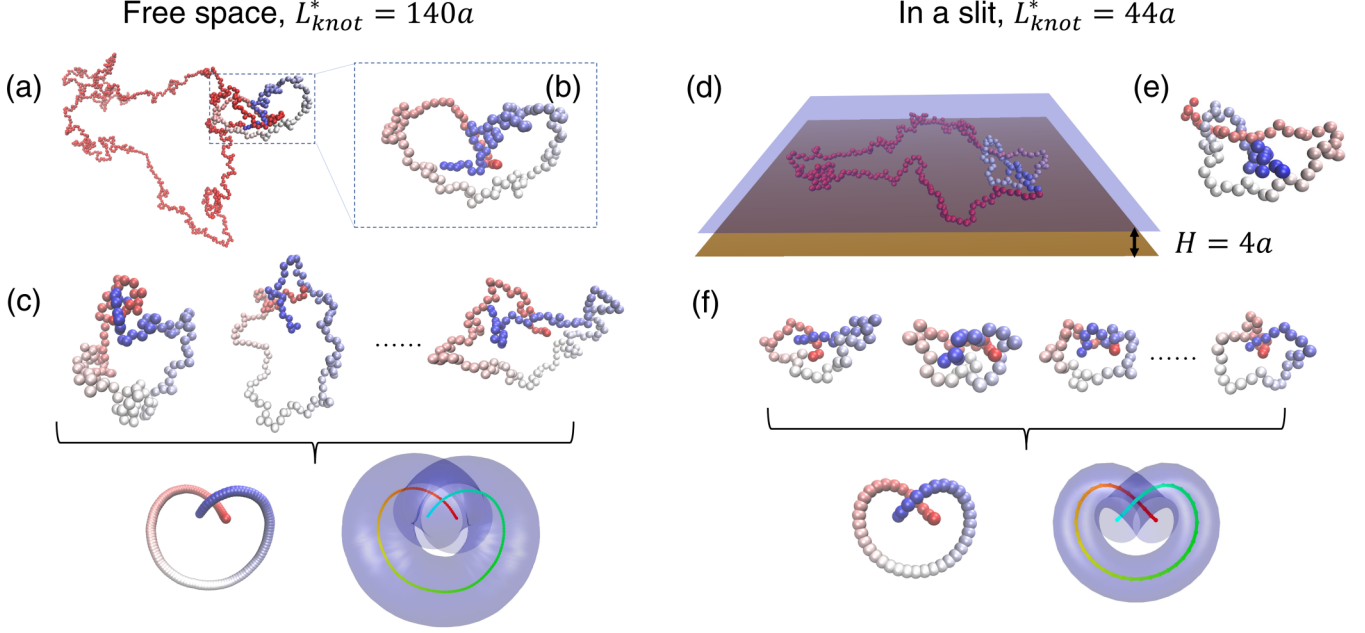
In a slit, $L^*_{knot} = 44a$

FIG. 1. The touching-bead model of polymer in our simulation and the illustration of the calculation of the knot tube. (a) A typical simulation snapshot of a knotted flexible chain with the most probable knot size polymer knot $L^*_{knot} = 140a$. (b) The knot core containing 140a monomers. (c) Superimposing many knot-core conformations to obtain the tube for knots. The bottom-left inset is the tube axis, and the bottom-right inset is the tube. (d)–(f) Similar images as (a)–(c) but for polymer knots in a slit with the slit height $H = 4a$.

the 2D case. Hence, our results can be applied to understand polymer knots on surface, such as DNA knots measured by atomic force microscopy (AFM) [56].

II. METHODS

A. Monte Carlo simulation of a knotted polymer

We perform Monte Carlo (MC) simulation to sample the equilibrium conformations of a circular knotted flexible chain. The circular chain is modeled by a string of touching beads [Fig. 1(a)] [57–59]. In the touching-bead model, the bond length between centers of two adjacent beads is fixed as a. The pairwise interaction between beads are described by a hardcore repulsion with the hardcore diameter of a:

$$E_{\text{pair}}(r) = \begin{cases} +\infty & r \leqslant a, \\ 0 & r > a \end{cases} \quad (1)$$

where r is the interbead distance. This hardcore repulsion is often referred to as excluded volume (EV) interaction. The interaction between one bead and the slit walls is also described by the hard repulsion:

$$E_{\text{wall}}(z) = \begin{cases} 0 & |z| \leqslant (H-a)/2, \\ +\infty & \text{otherwise} \end{cases} \quad (2)$$

where z is the bead coordinate in the direction perpendicular to the slit walls and H is the slit height. Unless otherwise specified, no bending energy is considered in most simulations. Only in a few simulations, we add the bending energy to investigate the effects of bending stiffness on polymer knots: $E_{\text{bend}}/(k_BT) = (1/2)\kappa\theta^2$, where θ is the bending angle formed by three adjacent beads, k_B is the Boltzmann constant, and T is the temperature. Unless otherwise specified, the results presented in this work are for $\kappa = 0$.

Each MC simulation starts with a flexible circular chain containing a trefoil knot with the same handedness (left-handed). In each MC step, we randomly select three adjacent beads from the chain and carry out a crankshaft trial move for the center bead of the three. The trial conformation is rejected or accepted based on the Metropolis criterion. Note that in the absence of the bending energy, the chain energy is either 0 or $+\infty$. So, the trial conformation is accepted if there is no bead-bead or bead-wall overlap. The reason why we only move one bead in each MC step is to preserve the topology of the polymer during simulation, i.e., the trefoil knot. Accordingly, all sampled conformations are left-handed trefoil knots. If we carry out the crankshaft move for a large fragment of the polymer, the topology can change, and the polymer can switch to unknotted conformations. In this situation, it is very inefficient to sample trefoil-knotted conformations when the equilibrium knotting probability is very low. For a polymer confined in a very narrow slit, the knotting probability becomes very small. As a result, in this work we move only one bead in each MC step. We typically run 10^{10} MC steps in each simulation and save conformations every 10^4 steps for analysis. We find that the correlation time of the knot size typically ranges from 10^7 to 10^8 MC steps. For each parameter set, the simulation time covers at least 100 correlation times.

In the simulations of polymer knots in slits, the chain lengths are $L = 200a$, $300a$, and $400a$, which are shorter than the typical chain length $L = 1000a$ in our previous studies [55,60]. It is because only one bead is moved in each MC step and the conformational evolution is slow in simulation. As mentioned above, such a MC move is to ensure that the trefoil knot is preserved during simulations. For comparison, we also perform simulations in free space with the chain length of $L = 1000a$, as shown in Fig. 1(a). In these

free-space simulations, crankshaft trial moves are implemented for large segments (containing many monomers) to speed up the simulations [55,60].

Two simulation animations are included in the Supplemental Material [61]. These two animations correspond to $L = 200a$, $H = 2a$ and $L = 400a$, $H = 3a$.

B. Knot analysis

We determine the knot core for a given polymer conformation using the Alexander polynomial [62]. The knot core is identified by cutting beads one by one from both ends until the knot type is changed. During this cutting process, the circular chain becomes open chains. Hence, we have to close both ends of an open chain before the calculation of the Alexander polynomial. Here we employ the minimally interfering closure scheme [63]. It is worth pointing out that a circular chain has no end, while the cutting-bead process requires knowing the chain ends. To solve this issue, we select four sites on the circular chain to sever as the chain ends. These four sites are evenly distributed along the chain. For each selection, we calculate the knot size L_{knot}, which is defined as the number of beads inside the knot core. Then we compare the four knot sizes calculated from four selections and save the smallest knot size as the final result and abandon the results from the other three selections. The reason for trying four sites to cut the circular chain is as follows. Before the knot analysis, we do not know the knot-core position. If we select only one site within the knot core to cut, we are not able to obtain the correct knot core, i.e., the smallest knot core. If we try four evenly distributed sites, at least one site should locate outside the knot core and allow us to determine the correct knot core considering that most knot sizes (knot contour lengths) are less than one half of the entire chain.

C. Calculation of the tubes for polymer knots

The algorithm to calculate the tubes for polymer knots have been presented in our recent studies [54,55,64]. Here we briefly describe the essential steps. We superimpose a large number ($> 10\,000$) of knot-core conformations [Fig. 1(f)] with the same L_{knot} and H to obtain the average conformation and fluctuations. Before superimposition, we fit the conformations through rotation and translation to minimize the deviations among structures. The fluctuations of individual knot-core conformations around the average knot-core conformation are used to determine tube diameters, while the average knot-core conformation is the tube axis. The tube radius, R_{tube}^{knot}, is defined as the root-mean-square deviation (RMSD) using the following equations:

$$R_{tube}(k) = \sqrt{\left[\frac{1}{N_{conf}}\sum_{i=1}^{N_{conf}} \|\vec{x}_i(k) - \vec{x}_{cen}(k)\|^2\right]},$$

$$\vec{x}_{cen}(k) = \frac{1}{N_{conf}}\sum_{i=1}^{N_{conf}} \vec{x}_i(k),$$

$$D_{tube}(k) \equiv 2R_{tube}(k), \tag{3}$$

where $k = 1, 2, \ldots, L_{knot}$ is the index of bead inside the knot core, $\vec{x}_i(k)$ is the 3D coordinates of the kth bead in the ith
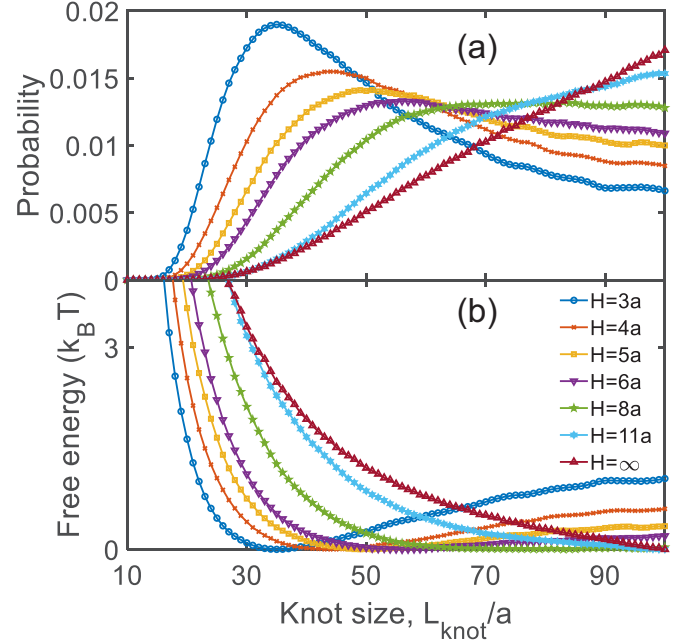

FIG. 2. (a) Probability of a trefoil knot at a given knot size L_{knot} on a knotted flexible chain with excluded volume interaction. (b) The potential of mean force as a function of the knot size calculated from the probabilities in (a) using Eq. (6).

conformation, N_{conf} is the number of knotted conformations, and $\vec{x}_{cen}(k)$ is the mean 3D coordinates (tube axis). Because the confinement is imposed along the z direction, we also calculate the fluctuation of knot-core conformations along the z direction:

$$R_{tube}^z(k) = \sqrt{\left[\frac{1}{N_{conf}}\sum_{i=1}^{N_{conf}} |z(k) - z_{cen}(k)|^2\right]},$$

$$z_{cen}(k) = \frac{1}{N_{conf}}\sum_{i=1}^{N_{conf}} z(k),$$

$$D_{tube}^z(k) \equiv 2R_{tube}^z(k), \tag{4}$$

where $z_i(k)$ is the z coordinates of knot-core conformations. We define

$$D_{tube}^{xy} \equiv \sqrt{(D_{tube})^2 - (D_{tube}^z)^2}. \tag{5}$$

The reason why the x and y directions are treated together because the tube cross section is two-dimensional (2D) and there is one additional dimension other than the z direction.

The precise calculation of the tubes for knots requires a large number of knot conformations and is computationally expensive. Hence, this work is focused on the trefoil knot.

III. RESULTS AND DISCUSSIONS

A. Knot shrinking in slit confinement

Figure 2 presents the size distributions of trefoil knots from the simulations of flexible chains confined in slits. Recall that the knot size, L_{knot}, is defined as the contour length of the polymer segment inside the knot core. The distribution of
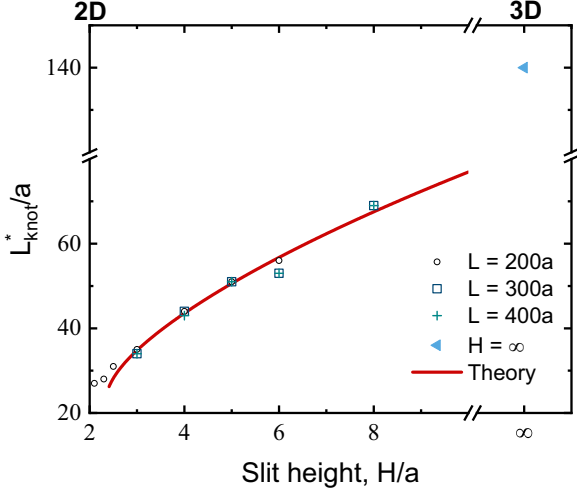
FIG. 3. The most probable knot size L_{knot}^* as a function of the slit height. Three symbols correspond to simulation results using three chain lengths. The solid line is the theoretical result using Eqs. (7)–(14).

L_{knot} has a peak at the most probable knot size, L_{knot}^*, which corresponds to the minimum of the free energy or the potential of mean force (PMF) [50,51]. The PMF is calculated from

$$\frac{F_{knot}^{sim}(L_{knot})}{k_B T} = -\ln[p(L_{knot})], \qquad (6)$$

where $p(L_{knot})$ is the relative probability of the trefoil knot at a given knot size from simulations, k_B is the Boltzmann constant, and T is the temperature. Note that the total knotting probability $\int_0^L p \, dL_{knot}$ equals unity because the topology of the chain is fixed at the trefoil knot.

Then we turn to the dependence of L_{knot}^* on the slit height, H. As shown in Fig. 3, with the decrease of H, L_{knot}^* becomes smaller. Comparison of L_{knot}^* from the simulations with three chain lengths of $L = 200a$, $300a$, and $400a$ indicates that L_{knot}^* is insensitive to L as long as $L \gg L_{knot}^*$ (see more comparisons of different L in Figs. S1–S3 in the Supplemental Material [61]). The insensitivity has also been observed in previous studies [51,52]. Such an insensitive to the entire chain length is due to the fact L_{knot}^* is a local property, which corresponds to localized knots. Such knot localization is an entropic effect, which has been extensively investigated previously [50,51,65,66]. For the visualization of these localized knots, two simulation animations are presented in the Supplemental Material [61]. It is worth noting that when L_{knot}^* becomes comparable with L, L_{knot}^* depends on L due to the finite-chain-length effect. In other words, only when the chain length is sufficient long, these local knots reach the long-chain-limit behavior. Our simulations with $L = 200a$, $300a$, and $400a$ should reach the long-chain limit for $H \leqslant 8a$ because the simulation results of L_{knot}^* collapse among the three chain lengths. Note that in free space, i.e., $H = +\infty$, L_{knot}^* is approximately $140a$ [52]. Here, in the smallest slit with $H = 2a$, L_{knot}^* is approximately $26a$. Overall, the slit confinement leads to dramatical knot shrinking. If we treat $H = 2a$ as the 2D case, then the most probable knot size shrinks by a factor of 5 ($140a$ vs $26a$) from the three-dimensional (3D) case to the

2D case. Note that in free space (3D), the most probable knot size is $140a$ in the presence of the EV interaction and is only $7a$ in the absence of the EV interaction as observed by the simulations by Katritch *et al.* [67]. The repulsion from the EV interaction dramatically swells knots because in the absence of EV interaction, the segments in knots are very close to each other and their distributions are very sensitive to the EV interaction. In the following subsections, we will explain this confinement-induced knot shrinking using the tube model.

B. Effect of slit confinement on the knot tubes

To provide a simplified view of how slit confinement affects polymer knots, we generate the tube for polymer knots (Figs. 4 and 5). While individual knot-core conformations are irregular, their average conformation, i.e., the tube axis, assumes a neat and beautiful heart shape. We can approximate that all knot-core conformations are confined in a tube. The tube axis sketches the shape of knot-core conformation, and the tube diameter characterize the fluctuations of knot-core conformations. In the following part, we will present the dependences of the tube on the knot size and the slit height, respectively.

Figure 4(a) displays the tubes for the polymer knots confined in a slit with $H = 5a$. Four tube images correspond to four knot sizes. The tube properties can be quantified by many geometric parameters about the tube axis and tube cross section. The size of tube axis is quantified by the maximum spans in three directions: S_x, S_y, and S_z [see illustration in the last inset of Fig. 4(a)]. The tube diameter is quantified by D_{tube}. Considering that the tube cross section becomes anisotropic under strong confinement, we separate the z component of the tube diameter, D_{tube}^z, which characterizes the z-component deviation of individual knot-core conformations with respect to the tube axis. We also define $D_{tube}^{xy} \equiv \sqrt{(D_{tube})^2 - (D_{tube}^z)^2}$. It is worth mentioning that our tube plotting program can draw only circular tube cross sections, including the tubes in Fig. 4(a) and other figures.

Figures 4(b)–4(g) show the variations of the tube parameters when varying the knot size at $H = 5a$. To better view the dependence of the tube axis on the knot size, we make 3D curves in Fig. 4(b) and two projections in Figs. 4(c) and 4(d). It is worth noting that in each tube, the tube diameter D_{tube} varies along the tube axis. We calculate an average tube diameter $\langle D_{tube} \rangle$ for each tube.

We observe several changes of the tube when varying L_{knot}. First, the maximum spans of the tube axis in the x and y directions, S_x and S_y, increase with L_{knot}. Second, the maximum span of the tube axis in the z direction, S_z, decrease with L_{knot} [Fig. 4(f)]. Third, $\langle D_{tube} \rangle$ increases almost linearly with L_{knot} [Fig. 4(f)]. Fourth, $\langle D_{tube}^z \rangle$ increases slowly with L_{knot}, while $\langle D_{tube}^{xy} \rangle$ increases rapidly with L_{knot}. The reasons for these changes, together with the reasons for other changes presented below, will be elaborated in the last part of this subsection.

Then we move to the dependence of the knot tube on the slit height. Figure 5 presents the data in the similar manner as Fig. 4, except that now we vary the slit height with a fixed knot size $L_{knot} = 60a$. With the decrease of H, both S_x and S_y become slightly larger [Fig. 5(c)], and S_z becomes
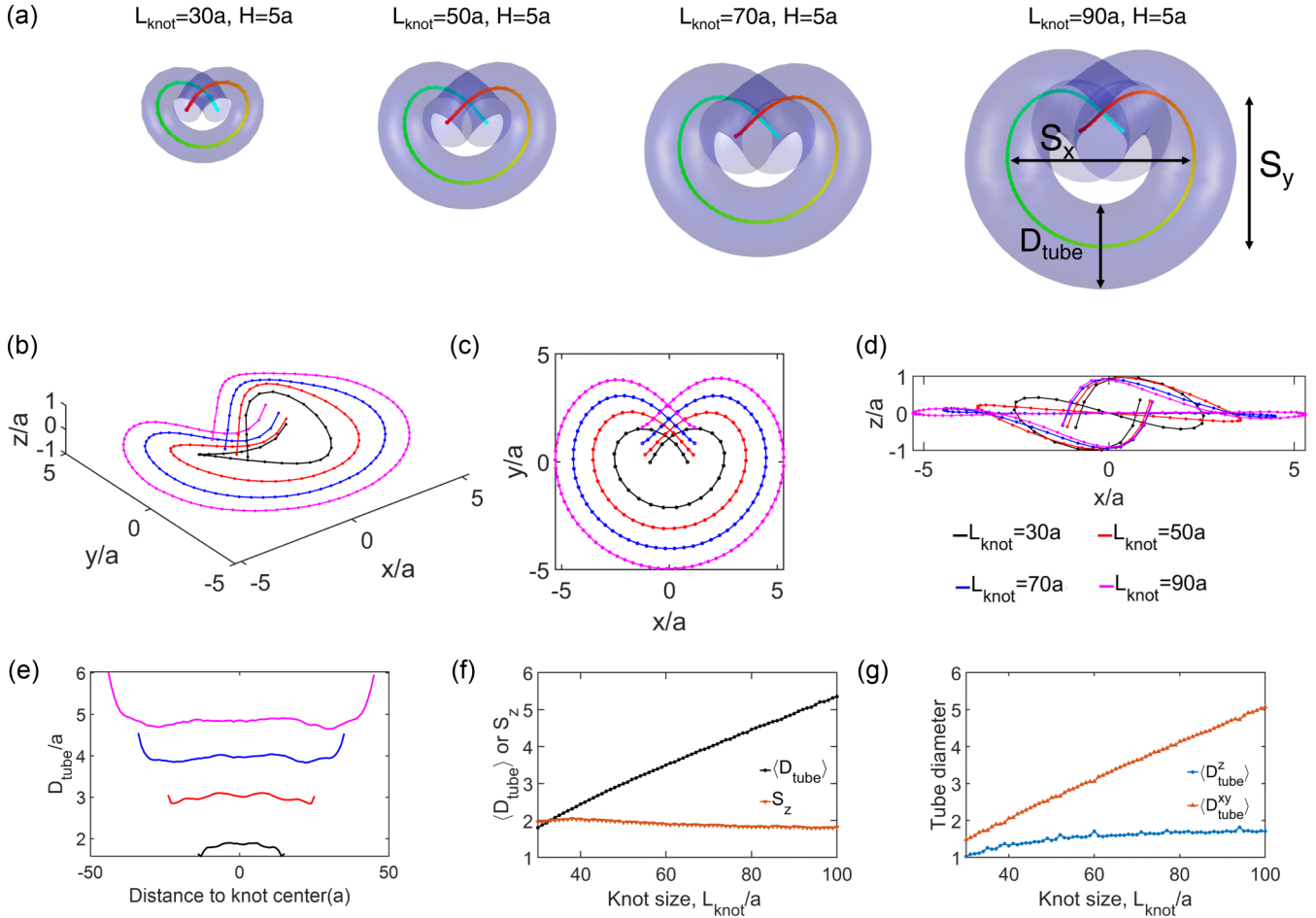
FIG. 4. Variation of the tube parameters when varying the knot size with a fixed height $H = 5a$. (a) Knot tubes for four knot sizes. (b) The 3D tube axes for four knot sizes. (c), (d) Projections of tube axes on the x-y and x-z planes. (e) The tube diameter along the tube axis. (f) Mean tube diameter and max z-span of the tube axis as a function of the knot size. (g) z component and xy component of the tube diameters.

larger [Figs. 5(d) and 5(f)]. It is intriguing that $\langle D_{\text{tube}} \rangle$ remains almost unchanged when varying H. Separation of the z and xy components of $\langle D_{\text{tube}} \rangle$ reveals that the slit confinement squeezes $\langle D_{\text{tube}}^z \rangle$ and expands $\langle D_{\text{tube}}^{xy} \rangle$ [Fig. 5(g)], which results in a nearly constant of $\langle D_{\text{tube}} \rangle$.

Figure 6 presents the tube parameters over wide ranges of L_{knot} and H. The average tube diameter increases almost linearly with L_{knot} for all slit heights from $H = +\infty$ to $H = 3a$. We define an aspect ratio for the knot tube: $p = L_{\text{knot}}/\langle D_{\text{tube}} \rangle$. The aspect ratio p varies slightly between 18 and 20 for a wide range of H. For comparison, a wormlike chain has an aspect ratio about 10 [54]. So the aspect ratio is larger in the case of flexible chains with excluded volume interactions. This is because flexible chains adopted more curved conformations than wormlike chains.

The dependence of S_z on L_{knot} is not simple. In free space, i.e., $H = +\infty$, S_z increases with L_{knot}. This is reasonable considering that a larger knot has a larger tube axis. In very strong confinement, e.g., $H = 3a$, S_z decreases with L_{knot}. As explained above, it is because the slit height restricts the sum of S_z and $\langle D_{\text{tube}}^z \rangle$. A large knot has a larger tube diameter, and hence S_z needs to be reduced to satisfy the restriction. For intermediate slit heights, e.g., $H = 6a$, S_z first increases

and then decreases with L_{knot}. The reason is as follows. The increase of S_z with L_{knot} occurs in the situation that the sum of S_z and $\langle D_{\text{tube}}^z \rangle$ does not reach the limit of the slit height so that both S_z and $\langle D_{\text{tube}} \rangle$ increases with L_{knot}. After the sum of S_z and $\langle D_{\text{tube}}^z \rangle$ reaches the limit of the slit height, S_z must decrease. Overall, placing a large knot in a slit must compress something, either the tube diameter or the tube axis. Our results suggest that the compression eventually is imposed on the tube axis instead of the tube diameter, probably because compressing the tube axis costs less than compressing the tube diameter. Such interpretation will be supported by more evidence shown below.

It might appear to be controversial that the average tube diameter is even larger than the slit height in Fig. 6(a). This is impossible for a tube with an isotropic cross section. The reason for this apparent controversy is that the tube cross section becomes anisotropic for a strongly compressed tube. It means that the tube cross section has a smaller dimension in the z direction than the one in the x or y direction. The tube cross section can even expand along the x or y direction to compensate the shrinking along the z direction. Recall that for a large knot, the tube axis spans widely in the x and y directions as indicated by the values of S_x and S_y, and hence
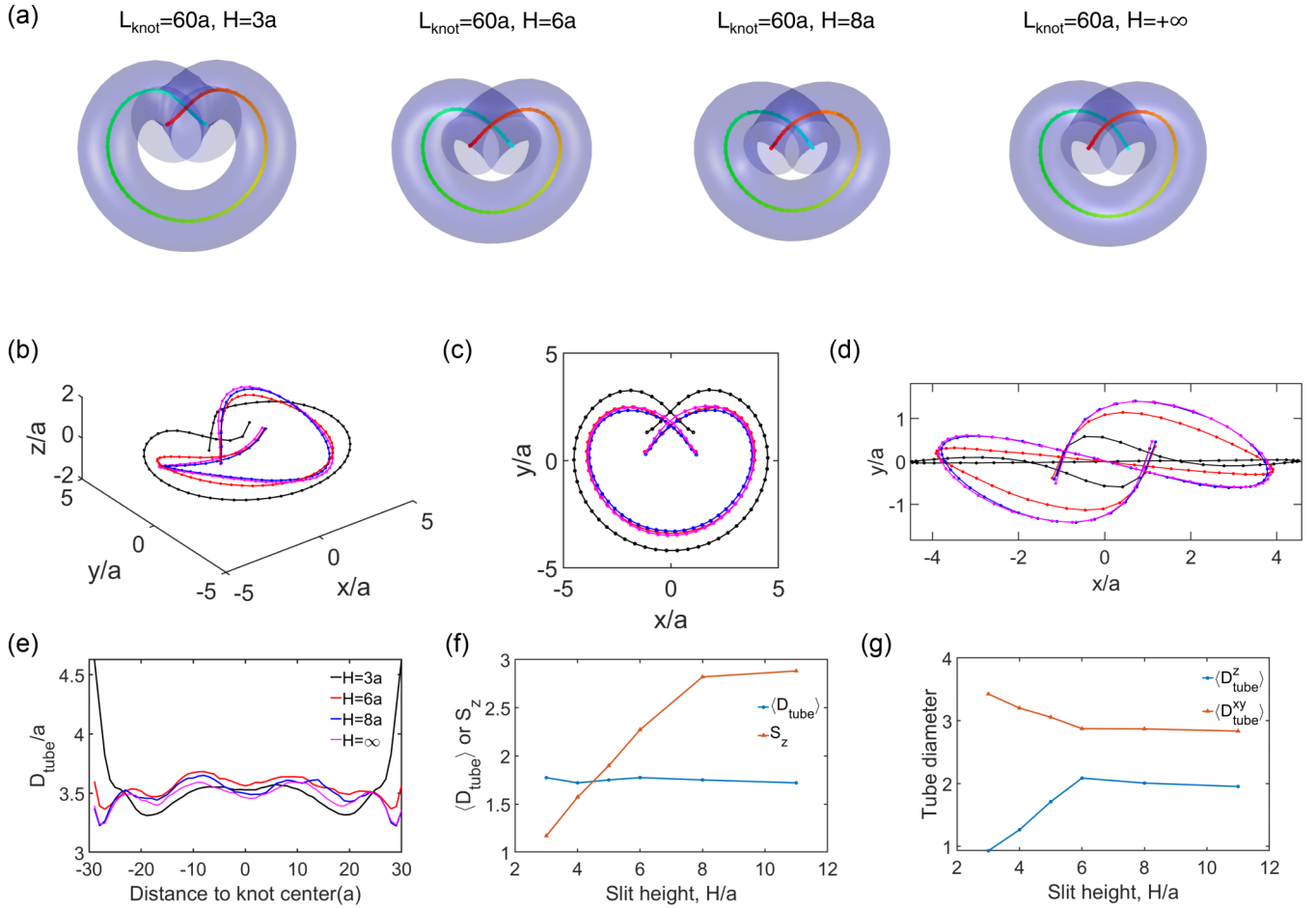
FIG. 5. Similar plots as Fig. 4 but for knots with a fixed knot size $L_{\text{knot}} = 60a$ and four different slit heights. Four colors in (c)–(e) correspond to four H values as indicated in the legend of (e).

there is plenty of room for the tube cross section to expand along the x and y directions.

Based on the results in Figs. 4–6, we draw an illustration in Fig. 7 to depict the slit-confinement effects on the knot tubes. Note that Fig. 7 considers the situation of varying the slit height with a fixed knot size. As shown in Fig. 7(a), with the decrease of the slit height from $H = +\infty$, the first slit-confinement effect is aligning the knot tubes, which mainly occurs in $S_z^{\text{free}} \lesssim H \lesssim (S_x^{\text{free}}$ and $S_y^{\text{free}})$. When H becomes less than S_z^{free}, the knot tubes are almost fully aligned with slit plates and the second slit-confinement effect is the compression of the knot tubes [Fig. 7(b)]. At first, S_z is reduced because the tube axis is relative easier to be compressed than the tube diameter, and then both S_z and D_{tube} are reduced, because the slit height cannot even accommodate the free-space value of D_{tube}^z. Our results in Fig. 5(g) indicates that D_{tube}^{xy} expands in strong slit confinement in order to maintain the conformational space of polymer knots. Note that for a large knot, the tube axis spans widely in the x and y directions as indicated by the values of S_x and S_y, and hence there is plenty of room for the tube cross section to expand along the x and y directions. Recall that Fig. 7 focuses on the situation that the knot size is fixed at a given value. The onset of the

knot-tube compression [Fig. 7(b)] is determined by S_x^{free}, S_y^{free}, and S_z^{free}, which depends on the knot size. Large knots feel the compression earlier than small knots and hence experience more confinement free energy. In other words, large knots are more disfavored in slits, which is the reason why knot population shifts toward small knots in slits.

C. Explanation of confined-induced knot shrinking using the tube model

Next, we apply the tube parameters obtained above to explain confined-induced knot shrinking. Before proceeding to the quantitative calculation, we first present the simple reason for confined-induced knot shrinking. The polymer segments inside the knot core experience more confinement free energy than the polymer segments out of the knot core, and hence expelling the polymer segments from the knot core to the outside region can lower the free energy of the entire chain. This expelling process tightens the knot, which needs to overcome the restoring force of a tightened knot. Eventually, an equilibrium knot size is resulted from the competition of the expelling force and restoring force. Both forces will be derived below.
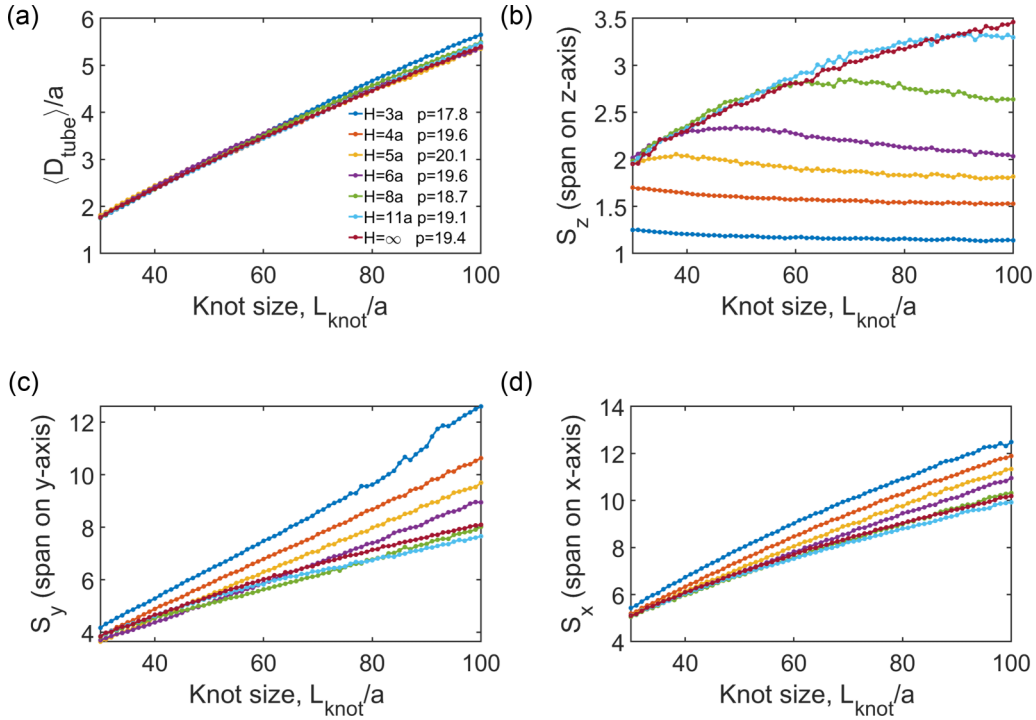
FIG. 6. (a) The average tube diameter varies with the knot size in different slit heights. (b)–(d) The max spans of the tube axis in three directions.

Following the above qualitative explanation, we write the free energy cost of forming a trefoil knot with the size L_{knot} in a slit, $F_{knot}^{slit}(L_{knot})$, as [48]

$$F_{knot}^{slit}(L_{knot}) = F_{knot}^{free}(L_{knot}) + F_{excess}(L_{knot}), \qquad (7)$$

$$F_{excess}(L_{knot}) \equiv F_{knot}^{wall}(L_{knot}) - F_{unknot}^{wall}(L_{knot}). \qquad (8)$$

In the above equations, $F_{knot}^{free}(L_{knot})$ is the free energy cost of knot formation in free space, $F_{knot}^{wall}(L_{knot})$ is the confinement free energy experienced by the knot in a slit, and $F_{unknot}^{wall}(L_{knot})$ is the confinement free energy experienced by the unknotted segments of length L_{knot} in a slit. The difference in confinement free energy between knotted and unknotted segments, $F_{excess}(L_{knot})$, is responsible for confinement-induced knot shrinking. The expelling force mentioned in the above
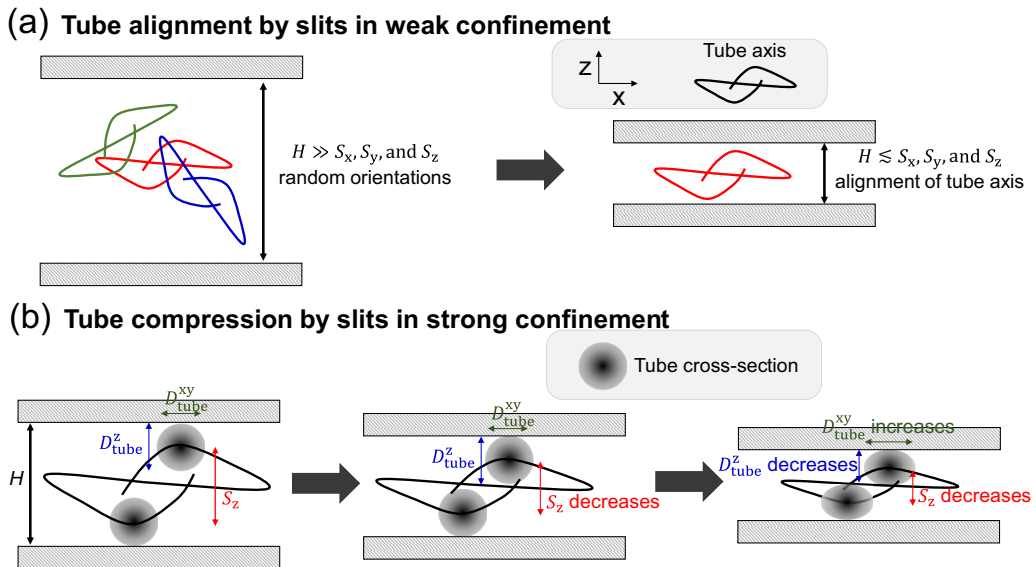

FIG. 7. Illustration of slit confinement on the knot tubes. (a) In free space or very wide slits, the tube orientations are nearly random. With the decrease of the slit height, the tube orientations become aligned. (b) Further decreasing the slit height compresses the knot tubes. The compression is first imposed on the tube axis along the z direction, S_z, and then the tube diameter along the z direction, D_{tube}^z. The shrinking of D_{tube}^z is accompanied with the expansion of D_{tube}^{xy}. This figure focuses on the situation that the knot size is fixed.

paragraph corresponds to $-\partial F_{\text{excess}}(L_{\text{knot}})/\partial L_{\text{knot}}$, and the restoring force corresponds to $-\partial F_{\text{knot}}^{\text{free}}(L_{\text{knot}})/\partial L_{\text{knot}}$.

Then we need to find out the expressions for $F_{\text{knot}}^{\text{free}}$, $F_{\text{knot}}^{\text{wall}}$, and $F_{\text{unknot}}^{\text{wall}}$. In our previous study [52], we have investigated the free energy cost of knot formation on a flexible chain in free space, but there is no analytical expression of $F_{\text{knot}}^{\text{free}}$. Here we obtain an approximate equation for $F_{\text{knot}}^{\text{free}}(L_{\text{knot}})$ based on connecting two asymptotic relationships in the small- and large-knot regimes:

$$F_{\text{m}}^{\text{free}} \equiv F_{\text{knot}}^{\text{free}}/L_{\text{knot}} \approx \frac{1}{e^{\frac{L_{\text{knot}}/a-47.5}{4}} + 1} F_{\text{small}}^{\text{free}}$$
$$+ \frac{e^{\frac{L_{\text{knot}}/a-47.5}{4}}}{e^{\frac{L_{\text{knot}}/a-47.5}{4}} + 1} F_{\text{large}}^{\text{free}}, \qquad (9)$$

$$F_{\text{small}}^{\text{free}}/(k_B T) \approx 0.0884 \ln \left(D_{\text{eff}}^2/12a^2 \right), \qquad (10)$$

$$\frac{F_{\text{large}}^{\text{free}}}{k_B T} \approx 0.256 \left(\frac{D_{\text{eff}}}{a} \right)^{-1.7}, \qquad ((11)$$

$$D_{\text{eff}} = L_{\text{knot}}/p - a. \qquad (12)$$

In the above equations, $F_{\text{m}}^{\text{free}}$ is the confinement free energy per monomer in the knot core, and $F_{\text{small}}^{\text{free}}$ and $F_{\text{large}}^{\text{free}}$ are the asymptotic relationships in the small- and large-knot regimes, respectively [52]. The two coefficients in front of $F_{\text{small}}^{\text{free}}$ and $F_{\text{large}}^{\text{free}}$ are used to smoothly connect the two asymptotic relationships. The two coefficients in Eqs. (10) and (11) are obtained from the fit to simulation results as shown in Fig. 8(a). In Eq. (12) we define an effective tube diameter $D_{\text{eff}} \equiv \langle D_{\text{tube}} \rangle - a$ and $\langle D_{\text{tube}} \rangle = L_{\text{knot}}/p$, considering that the excluded volume interaction decreases the accessible tube diameter [52]. As shown by Fig. 8(a), $F_{\text{m}}^{\text{free}}$ calculated from Eq. (9) can quantitatively agree with the simulation result.

After obtaining an expression for $F_{\text{knot}}^{\text{free}}$, we turn to F_{excess} in Eq. (7), which consists of two terms: $F_{\text{knot}}^{\text{wall}}$ and $F_{\text{unknot}}^{\text{wall}}$. We propose two empirical expressions for $F_{\text{knot}}^{\text{wall}}$ and $F_{\text{unknot}}^{\text{wall}}$ based on the fit to simulation results:

$$F_{\text{knot}}^{\text{wall}}/(k_B T) \approx 7.7 \frac{(L_{\text{knot}} - pa)^{1/3} a^{2/3}}{H_{\text{eff}}}, \qquad (13)$$

$$F_{\text{unknot}}^{\text{wall}}/(k_B T) \approx 0.205 \frac{L_{\text{knot}} a}{H_{\text{eff}}^2}, \qquad (14)$$

$$H_{\text{eff}} \equiv H - a. \qquad (15)$$

As shown by Fig. 8(c), the above two equations can quantitatively capture the simulation results of $F_{\text{excess}}(L_{\text{knot}})$, which is calculated from the difference of potentials of mean force (PMF) in free space and in a slit. The examples of PMFs are presented in Fig. 2(b). Besides $H = 5a$, we compare the simulation results and theoretical predictions of F_{excess} for other slit heights in Fig. S4 of the Supplemental Material [61].

The functional form in Eq. (13) can be understood in this way. As explained above, the compression of the knot tube by slit confinement is mainly imposed on the dimension of the tube axis along the z direction, S_z. The free energy cost of compressing the tube axis is approximately characterized by Eq. (13) using the following analysis. As shown in Fig. 8(b), in free space, S_z^{free} can be well fitted by $S_z^{\text{free}}(L_{\text{knot}}) = 0.726(L_{\text{knot}} - pa)^{1/3} a^{2/3} + 0.320$, which shares
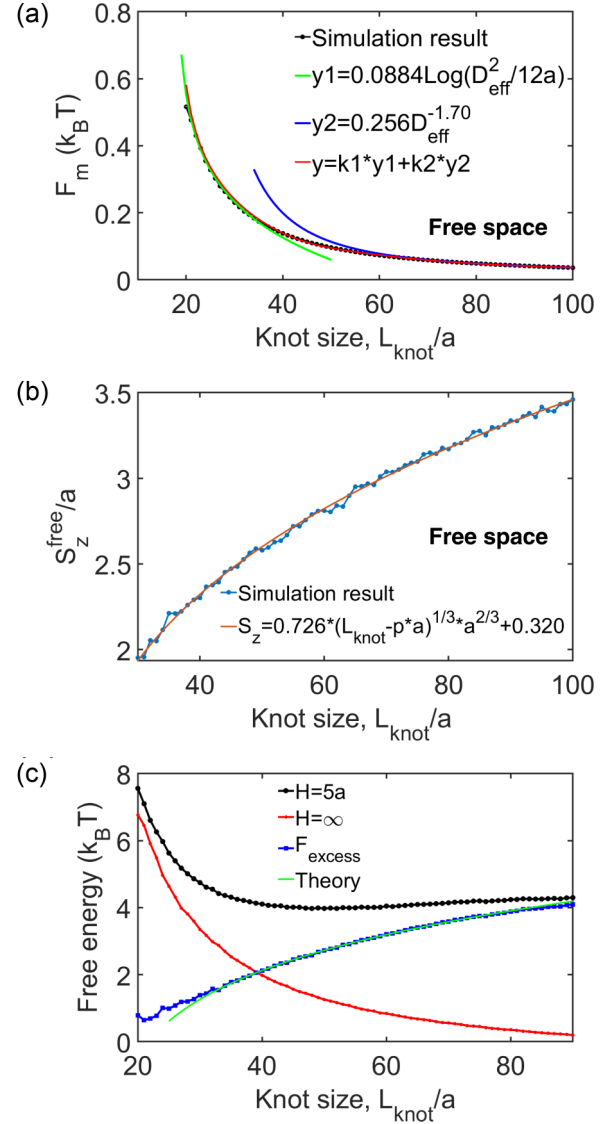

FIG. 8. Effect of slit confinement on the free energy of polymer knots. (a) The free energy cost $F_{\text{knot}}^{\text{free}}(L_{\text{knot}})$ of forming a trefoil knot with the knot size L_{knot} on a flexible chain with excluded volume interaction in free space. Here the y axis corresponds to the free energy per monomer, which is defined as $F_{\text{m}} \equiv F_{\text{knot}}^{\text{free}}/L_{\text{knot}}$. (b) The max span of the tube axis along the z direction for trefoil knots in flexible chains with excluded volume interaction in free space. (c) The free energies of a knot in free space and in the slit $H = 5a$ and their difference. The theoretical curve (green) is calculated from Eqs. (13) and (14).

the same functional form as the denominator in Eq. (13) except a constant term. It is reasonable that the compression free energy cost is determined by the ratio of S_z^{free} to H_{eff}. Note that due to the hardcore diameter of beads (monomers), the accessible slit height is $H_{\text{eff}} \equiv H - a$ instead of H. The same reasoning can be applied to understand the functional form in Eq. (14) for the compressed free energy cost of unknotted segments of length L_{knot}. A random walk over the contour length of L_{knot} spans about $\sqrt{L_{\text{knot}}a}$ in free space and is compressed into a space with the height of H_{eff}. It is worth noting that although the functional forms in Eqs. (13) and (14)
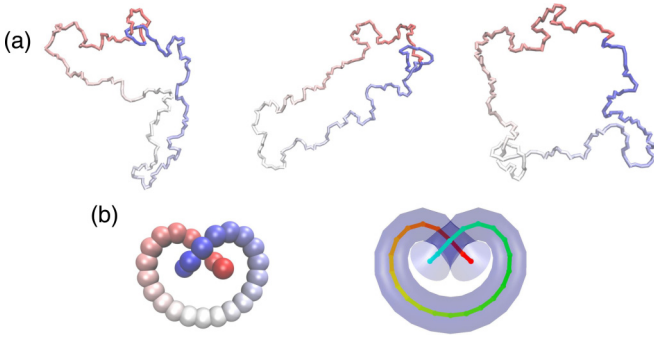
FIG. 9. Polymer knots in the extreme case with $H = 2a$ (the 2D case). (a) Three simulation snapshots of flexible knotted polymers with $L = 200a$. (b) The knot tube for the most probable knot size $L_{\text{knot}}^* \approx 26a$.

are empirical to a large extent, both equations have reasonable physical meanings and work well to explain the simulation results in Fig. 8.

Substituting Eqs. (9)–(15) into Eq. (7) and minimizing $F_{\text{knot}}^{\text{slit}}$ with respect to L_{knot} for each H, we obtain the dependence of L_{knot}^* on H, which fairly agrees with the simulation results as shown in Fig. 3. Overall, our theoretical prediction is based on the physical picture that F_{excess} tends to squeeze a knot, which is eventually balanced with the restoring force of a compressed knot.

D. Understanding a polymer knot on a surface through the extreme case of $H = 2a$.

With the decrease of the slit height from $H = +\infty$ to $H = 2a$, the confined polymer gradually changes from the 3D case to the 2D case. Accordingly, the slit confinement provides a unique property to investigate the polymer knots in the 2D case or on a surface. Our analysis gives not only the knot properties in the 2D case but also how 2D polymer knots evolve from 3D polymer knots through the slit confinement.

Recall that to accommodate the crossing of two polymer segments, the minimum slit height is $H_{\text{min}} = 2a$. The exact H_{min} value can be slightly lower than $2a$ considering the grooves between two adjacent beads. Note that the sampling efficient of polymer conformations dramatically decreases as the slit height approaches to H_{min}. The smallest slit height considered here is $2a$.

Figure 9(a) displays the simulation snapshots of knotted polymers and the knot tube for $H = 2a$. The most probable knot size is $(L_{\text{knot}}^*)_{2D} \approx 26a$, and the corresponding tube diameter is $\langle D_{\text{tube}} \rangle_{2D} \approx 1.63a$. The z component is $\langle D_{\text{tube}} \rangle_{2D} \approx 0.54a$. The average knot conformation and the tube for $(L_{\text{knot}}^*)_{2D} \approx 26a$ are shown in Fig. 9(b). Recall that our tube plotting program can only draw circular tube cross sections, including the tubes in Fig. 9. The average knot conformation has the maximum spans in three dimensions as $S_x \approx 5.35a$, $S_y \approx 4.14a$, and $S_z \approx 0.912a$. For the visualization of the knots at $H = 2a$, a simulation animation is presented in the Supplemental Material [61].

Our results of the polymer knots on a surface may be applied to understand DNA knots on a surface measured by AFM [56]. However, we must consider two major differences

between our simulations and AFM experiments when comparing these two cases. First, in our simulations, the polymers are pushed to the 2D case by spatial confinement and assume equilibrium 2D conformations. In AFM experiments, DNA molecules are absorbed on the surface due to the DNA-surface attraction. Depending on the attractive strength, these DNA molecules can assume equilibrium 2D conformations for weak attractions or frozen 2D conformations for strong attractions. Experimentalists have recently developed methods to tune the attractive strength between DNA molecules and the surface, mainly through controlling the salt specie and concentration or chemical modification of the surface [68,69]. When the attractions between DNA molecules and the surface are sufficiently weak, DNA conformations on the surface can be considered to be fully relaxed, i.e., reach equilibrium 2D conformations, which has been validated by quantitative analysis of these DNA conformations [68,69]. In such cases, equilibrated DNA conformations on the surface should be quite close to the polymer conformations confined between two plates with $H = 2a$.

Second, in our simulations, polymers are flexible chains, while double-stranded DNA molecules are semiflexible chains. When using $E_{\text{bend}}/(k_B T) = (1/2)\kappa \theta^2$ for the bending energy in our polymer simulations, the bending stiffness of DNA is typically between 10 and 25 depending on the ionic strength [70]. As mentioned in the method section, the simulations with a large κ require long chains to cover the most knot sizes and are very computationally expensive. To get an idea about how the bending stiffness affects the knot tube, we compare the simulation results for $\kappa = 0$, 1, and 2 with $H = 6a$ and $L_{\text{knot}} = 60a$. See Fig. S5 in the Supplemental Material [61]. We use $H = 6a$ instead of $H = 2a$ because the sampling efficiency for $H = 2a$ and $\kappa > 0$ is too low. We find that $\langle D_{\text{tube}} \rangle$ increases rapidly with κ. It is very computationally expensive to further increase κ to the value corresponding to double-stranded DNA. For example, supposing that $L_p \approx 50$ nm and the effective DNA diameter $a \approx 2.5$ nm, we have $\kappa \approx 20$ [70]. To obtain the long-chain limit of the knots, $L \gg L_{\text{knot}}^*$ should be satisfied. It is probably computationally impractical to simulate a long chain with L on the order of thousand in strong confinement with $H \approx 2a$ using the touching-bead model. Other polymer models or other conformational sampling methods may be employed to obtain the knot properties of a semiflexible chain with large κ in strong confinement with $H \approx 2a$.

IV. CONCLUSIONS

In conclusion, the effects of slit confinement on polymer knots are quantified and analyzed using the tube model. The most probable knot size dramatically shrinks from $(L_{\text{knot}}^*)_{3D} \approx 140a$ at $H = +\infty$ to $(L_{\text{knot}}^*)_{2D} \approx 26a$ at $H = 2a$. The reason for confined-induced knot shrinking is as follows. Compared to monomers outside the knot core, monomers in the knot core experience more confinement free energy due to segment crossings. As a result, the polymer expels monomers from the knot core to the outside region to lower the free energy of the entire chain. Quantification of the knot tubes reveals that to squeeze a large knot tube into a slit, the compression is mainly imposed on the tube axis rather than the tube diameter. When

the slit height is too small to accommodate the tube diameter, the tube cross section is compressed along the z direction while the tube cross section maintains its dimensions along the x and y directions.

This work also demonstrates that the tube model provides a simplified view of the polymer knots, which usually appear irregular and disorder. Using the tube model, we can imagine that these polymer knot conformations are confined in heart-shape tubes. Then the confinement effects can be understood through the deformation of the knot tubes.

It is worth pointing out that our algorithm of calculating the tubes for knots strongly relies on the fact that the knots have well-defined shapes, which allows us to superimpose equilibrium knot-core conformations to obtain the tubes. For unknotted polymer segments and interchain entanglements in polymer melts, our algorithm is not applicable, because there is often no well-defined shape and hence superimposing many random conformations leads to a single structureless point.

The significance of this work lies in both fundamental and practical aspects. From the fundamental viewpoint, the slit confinement bridges the polymer knots in the 3D and 2D cases, which allows us to understand the differences of polymer knots in the 3D and 2D cases. It is worth pointing out that our model of flexible chains are essentially self-avoiding walks (SAWs), and so our results reveal generic properties of knotting in 3D and 2D SAWs. From the practical viewpoint, our results can be applied to understand DNA knots in biological and experimental systems, in particular, DNA in AFM [56] and nanofluidic experiments [36,38,39,45].

ACKNOWLEDGMENTS

[1] V. P. Patil, J. D. Sandt, M. Kolle, and J. Dunkel, Topological mechanics of knots and tangles, Science **367**, 71 (2020).

[2] E. Ben-Naim, Z. Daya, P. Vorobieff, and R. E. Ecke, Knots and Random Walks in Vibrated Granular Chains, Phys. Rev. Lett. **86**, 1414 (2001).

[3] A. Belmonte, M. J. Shelley, S. T. Eldakar, and C. H. Wiggins, Dynamic Patterns and Self-Knotting of a Driven Hanging Chain, Phys. Rev. Lett. **87**, 114301 (2001).

[4] D. M. Raymer and D. E. Smith, Spontaneous knotting of an agitated string, Proc. Natl. Acad. Sci. USA **104**, 16432 (2007).

[5] M. A. Krasnow, A. Stasiak, S. J. Spengler, F. Dean, T. Koller, and N. R. Cozzarelli, Determination of the absolute handedness of knots and catenanes of DNA, Nature (London) **304**, 559 (1983).

[6] A. Stasiak, V. Katritch, J. Bednar, D. Michoud, and J. Dubochet, Electrophoretic mobility of DNA knots, Nature (London) **384**, 122 (1996).

[7] V. V. Rybenkov, N. R. Cozzarelli, and A. V. Vologodskii, Probability of DNA knotting and the effective diameter of the DNA double helix, Proc. Natl. Acad. Sci. USA **90**, 5307 (1993).

[8] S. Y. Shaw and J. C. Wang, Knotting of a DNA chain during ring closure, Science **260**, 533 (1993).

[9] X. R. Bao, H. J. Lee, and S. R. Quake, Behavior of Complex Knots in Single DNA Molecules, Phys. Rev. Lett. **91**, 265506 (2003).

[10] W. R. Taylor, A deeply knotted protein structure and how it might fold, Nature (London) **406**, 916 (2000).

[11] N. C. Lim and S. E. Jackson, Molecular knots in biology and chemistry, J. Phys. Condens. Matter **27**, 354101 (2015).

[12] M. Jamroz, W. Niemyska, E. J. Rawdon, A. Stasiak, K. C. Millett, P. Sułkowski, and J. I. Sulkowska, KnotProt: A database of proteins with knots and slipknots, Nucleic Acids Res. **43**, D306 (2014).

[13] Y.-L. Lai, C.-C. Chen, and J.-K. Hwang, pKNOT v. 2: The protein KNOT web server, Nucleic Acids Res. **40**, W228 (2012).

[14] A. Bustamante, J. Sotelo-Campos, D. G. Guerra, M. Floor, C. A. Wilson, C. Bustamante, and M. Báez, The energy cost of polypeptide knot formation and its folding consequences, Nat. Commun. **8**, 1581 (2017).

[15] A. L. Mallam and S. E. Jackson, Knot formation in newly translated proteins is spontaneous and accelerated by chaperonins, Nat. Chem. Biol. **8**, 147 (2012).

[16] F. Ziegler, N. C. Lim, S. S. Mandal, B. Pelz, W.-P. Ng, M. Schlierf, S. E. Jackson, and M. Rief, Knotting and unknotting of a protein in single molecule experiments, Proc. Natl. Acad. Sci. USA **113**, 7533 (2016).

[17] Á. San Martín, P. Rodriguez-Aliaga, J. A. Molina, A. Martin, C. Bustamante, and M. Baez, Knots can impair protein degradation by ATP-dependent proteases, Proc. Natl. Acad. Sci. USA **114**, 9864 (2017).

[18] T. Wüst, D. Reith, and P. Virnau, Sequence Determines Degree of Knottedness in a Coarse-Grained Protein Model, Phys. Rev. Lett. **114**, 028102 (2015).

[19] E. Orlandini, Statics and dynamics of DNA knotting, J. Phys. A **51**, 053001 (2017).

[20] C. Micheletti, D. Marenduzzo, and E. Orlandini, Polymers with spatial or topological constraints: Theoretical and computational results, Phys. Rep. **504**, 1 (2011).

[21] J. B. Schvartzman, P. Hernández, D. B. Krimer, J. Dorier, and A. Stasiak, Closing the DNA replication cycle: From simple circular molecules to supercoiled and knotted DNA catenanes, Nucleic Acids Res. **47**, 7182 (2019).

[22] T. Christian, R. Sakaguchi, A. P. Perlinska, G. Lahoud, T. Ito, E. A. Taylor, S. Yokoyama, J. I. Sulkowska, and Y.-M. Hou, Methyl transfer by substrate signaling from a knotted protein fold, Nat. Struct. Mol. Biol. **23**, 941 (2016).

[23] J. Tang, N. Du, and P. S. Doyle, Compression and self-entanglement of single DNA molecules under uniform electric field, Proc. Natl. Acad. Sci. USA **108**, 16153 (2011).

[24] C. B. Renner and P. S. Doyle, Stretching self-entangled DNA molecules in elongational fields, Soft Matter **11**, 3105 (2015).

[25] Y. Arai, R. Yasuda, K.-i. Akashi, Y. Harada, H. Miyata, K. Kinosita Jr, and H. Itoh, Tying a molecular knot with optical tweezers, Nature (London) **399**, 446 (1999).

[26] A. M. Saitta, P. D. Soper, E. Wasserman, and M. L. Klein, Influence of a knot on the strength of a polymer strand, Nature (London) **399**, 46 (1999).

[27] T. Stauch and A. Dreuw, Knots "choke off" polymers upon stretching, Angew. Chem. Int. Ed. **55**, 811 (2016).

[28] A. Rosa, M. Di Ventra, and C. Micheletti, Topological Jamming of Spontaneously Knotted Polyelectrolyte Chains Driven Through a Nanopore, Phys. Rev. Lett. **109**, 118301 (2012).

[29] C. Plesa, D. Verschueren, S. Pud, J. van der Torre, J. W. Ruitenberg, M. J. Witteveen, M. P. Jonsson, A. Y. Grosberg, Y. Rabin, and C. Dekker, Direct observation of DNA knots using a solid-state nanopore, Nat. Nanotech. **11**, 1093 (2016).

[30] A. Suma and C. Micheletti, Pore translocation of knotted DNA rings, Proc. Natl. Acad. Sci. USA **114**, E2991 (2017).

[31] R. K. Sharma, I. Agrawal, L. Dai, P. S. Doyle, and S. Garaj, Complex DNA knots detected with a nanopore sensor, Nat. Commun. **10**, 4473 (2019).

[32] R. K. Sharma, I. Agrawal, L. Dai, P. Doyle, and S. Garaj, DNA knot malleability in single-digit nanopores, Nano Lett. **21**, 3772 (2021).

[33] J. Arsuaga, M. Vázquez, S. Trigueros, and J. Roca, Knotting probability of DNA molecules confined in restricted volumes: DNA knotting in phage capsids, Proc. Natl. Acad. Sci. USA **99**, 5373 (2002).

[34] D. Marenduzzo, E. Orlandini, A. Stasiak, L. Tubiana, and C. Micheletti, DNA–DNA interactions in bacteriophage capsids are responsible for the observed DNA knotting, Proc. Natl. Acad. Sci. USA **106**, 22269 (2009).

[35] Y. Teng, N. T. Andersen, and J. Z. Chen, Statistical properties of a slit-confined wormlike chain of finite length, Macromolecules **54**, 8008 (2021).

[36] S. Amin, A. Khorshid, L. Zeng, P. Zimny, and W. Reisner, A nanofluidic knot factory based on compression of single DNA in nanochannels, Nat. Commun. **9**, 1506 (2018).

[37] W. Reisner, J. N. Pedersen, and R. H. Austin, DNA confinement in nanochannels: Physics and biological applications, Rep. Prog. Phys. **75**, 106601 (2012).

[38] Z. Ma and K. D. Dorfman, Diffusion of knots along DNA confined in nanochannels, Macromolecules **53**, 6461 (2020).

[39] Z. Ma and K. D. Dorfman, Diffusion of knotted DNA molecules in nanochannels in the extended de Gennes regime, Macromolecules **54**, 4211 (2021).

[40] J. Z. Chen and D. Sullivan, Free energy of a wormlike polymer chain confined in a slit: Crossover between two scaling regimes, Macromolecules **39**, 7769 (2006).

[41] R. Matthews, A. Louis, and J. Yeomans, Confinement of knotted polymers in a slit, Mol. Phys. **109**, 1289 (2011).

[42] C. Micheletti and E. Orlandini, Numerical study of linear and circular model DNA chains confined in a slit: Metric and topological properties, Macromolecules **45**, 2113 (2012).

[43] E. Orlandini and C. Micheletti, Knotting of linear DNA in nano-slits and nano-channels: A numerical study, J. Biol. Phys **39**, 267 (2013).

[44] R. Metzler, W. Reisner, R. Riehn, R. Austin, J. Tegenfeldt, and I. M. Sokolov, Diffusion mechanisms of localised knots along a polymer, EPL (Europhys. Lett.) **76**, 696 (2006).

[45] B. W. Soh and P. S. Doyle, Equilibrium conformation of catenated DNA networks in slitlike confinement, ACS Macro Lett. **10**, 880 (2021).

[46] A. R. Klotz, B. W. Soh, and P. S. Doyle, Motion of Knots in DNA Stretched by Elongational Fields, Phys. Rev. Lett. **120**, 188003 (2018).

[47] L. Dai, J. R. van der Maarel, and P. S. Doyle, Effect of nanoslit confinement on the knotting probability of circular DNA, ACS Macro Lett. **1**, 732 (2012).

[48] L. Dai, C. B. Renner, and P. S. Doyle, Metastable knots in confined semiflexible chains, Macromolecules **48**, 2812 (2015).

[49] A. Y. Grosberg, A. Feigel, and Y. Rabin, Flory-type theory of a knotted ring polymer, Phys. Rev. E **54**, 6618 (1996).

[50] A. Y. Grosberg and Y. Rabin, Metastable Tight Knots in a Wormlike Polymer, Phys. Rev. Lett. **99**, 217801 (2007).

[51] L. Dai, C. B. Renner, and P. S. Doyle, Metastable tight knots in semiflexible chains, Macromolecules **47**, 6135 (2014).

[52] L. Dai, C. B. Renner, and P. S. Doyle, Origin of Metastable Knots in Single Flexible Chains, Phys. Rev. Lett. **114**, 037801 (2015).

[53] L. Dai and P. S. Doyle, Effects of intrachain interactions on the knot size of a polymer, Macromolecules **49**, 7581 (2016).

[54] L. Dai, Developing the Tube Theory for Polymer Knots, Phys. Rev. Research **2**, 022014 (2020).

[55] L. Lu, H. Zhu, Y. Lu, L. An, and L. Dai, Application of the tube model to explain the unexpected decrease in polymer bending energy induced by knot formation, Macromolecules **53**, 9443 (2020).

[56] E. Ercolini, F. Valle, J. Adamcik, G. Witz, R. Metzler, P. De Los Rios, J. Roca, and G. Dietler, Fractal Dimension and Localization of DNA Knots, Phys. Rev. Lett. **98**, 058102 (2007).

[57] L. Dai, J. J. Jones, J. R. van der Maarel, and P. S. Doyle, A systematic study of DNA conformation in slitlike confinement, Soft Matter **8**, 2972 (2012).

[58] L. Dai, C. B. Renner, and P. S. Doyle, The polymer physics of single DNA confined in nanochannels, Adv. Colloid Interface Sci. **232**, 80 (2016).

[59] Y. Wang, D. R. Tree, and K. D. Dorfman, Simulation of DNA extension in nanochannels, Macromolecules **44**, 6594 (2011).

[60] H. Zhu, F. Tian, L. Sun, S. Wang, and L. Dai, Revisiting the non-monotonic dependence of polymer knotting probability on the bending stiffness, Macromolecules **54**, 1623 (2021).

[61] See Supplemental Material at http://link.aps.org/supplemental/10.1103/PhysRevE.105.024501 for simulation results of different chain lengths; comparion of simulation and theory for different slit heights; simulation results of polymers with bending stiffness; and two examples of simulation animations.

[62] M. Frank-Kamenetskiĭ and A. Vologodskiĭ, Topological aspects of the physics of polymers: The theory and its biophysical applications, Sov. Phys. Usp. **24**, 679 (1981).

[63] L. Tubiana, E. Orlandini, and C. Micheletti, Probing the entanglement and locating knots in ring polymers: A comparative study of different arc closure schemes, Prog. Theor. Phys. Suppl. **191**, 192 (2011).

[64] L. Dai, Tube model for polymer knots with excluded volume interactions and its applications, Macromolecules **54**, 9299 (2021).

[65] B. Marcone, E. Orlandini, A. Stella, and F. Zonta, What is the length of a knot in a polymer?, J. Phys. A: Math. Theor. **38**, L15 (2004).

[66] B. Marcone, E. Orlandini, and A. Stella, Knot localization in adsorbing polymer rings, Phys. Rev. E **76**, 051804 (2007).

[67] V. Katritch, W. K. Olson, A. Vologodskii, J. Dubochet, and A. Stasiak, Tightness of random knotting, Phys. Rev. E **61**, 5545 (2000).

[68] M. Sushko, A. Shluger, and C. Rivetti, Simple model for DNA adsorption onto a mica surface in 1:1 and 2:1 electrolyte solutions, Langmuir **22**, 7678 (2006).

[69] P. R. Heenan and T. T. Perkins, Imaging DNA equilibrated onto mica in liquid using biochemically relevant deposition conditions, ACS Nano **13**, 4220 (2019).

[70] C.-C. Hsieh, A. Balducci, and P. S. Doyle, Ionic effects on the equilibrium dynamics of DNA confined in nanoslits, Nano Lett. **8**, 1683 (2008).